



OPEN Nonlinear changes in urban heat island intensity, urban breeze intensity, and urban air pollutant concentration with roof albedo

Kyeongjoo Park & Jong-Jin Baik

This study systematically examines how the urban heat island (UHI) and urban breeze circulation (UBC) respond to an increase in roof albedo (α_r) and its influence on urban air pollutant dispersion. For this, idealized ensemble simulations are performed using the Weather Research and Forecasting (WRF) model. The increase in α_r from 0.20 to 0.65 decreases the UHI intensity, UBC intensity, and urban planetary boundary layer (PBL) height in the daytime (from 1200 to 1700 LST) by 47%, 36%, and 6%, respectively. As both UBC intensity and urban PBL height decrease, the daytime urban near-surface passive tracer concentration increases by 115%. The daytime UHI intensity, UBC intensity, and urban tracer concentration nonlinearly change with α_r : For $0.10 \leq \alpha_r < 0.80$, the rates of changes in the UHI intensity, UBC intensity, and urban tracer concentration with α_r overall increase as α_r increases. For $\alpha_r \geq 0.80$, the daytime roof surface temperature is notably lower than the daytime urban near-surface air temperature, the UHI intensity, UBC intensity, and urban tracer concentration very slightly changing with α_r . This study provides insights into the associations between changes in roof surface temperature and roof surface energy fluxes with α_r and those in UHI intensity.

Keywords Roof albedo, Urban heat island, Urban breeze circulation, Pollutant dispersion, Urban air quality, Cool roof

Although urban areas account for only about 3% of the world's total land area, urban areas now house more than 50% of the world's population^{1,2}. Dense populations and numerous infrastructures in urban areas result in significant modifications in local climates^{3,4}. In particular, urban areas typically exhibit higher near-surface air temperature than their surrounding rural areas, which is called the urban heat island (UHI)⁵. The UHI is known to have adverse health effects on urban residents in warm seasons^{6,7}. According to Lowe⁸, the UHI may increase heat-related deaths by 1.1 people per million in U.S. cities. Moreover, the adverse effects of the UHI are expected to be intensified with climate change and increasing heat wave occurrences, which necessitates an effective UHI mitigation strategy^{9,10}.

To alleviate the UHI, various mitigation strategies have been suggested¹¹. Among them, the cool roof (reflective roof) is one of the most widely adopted UHI mitigation measures¹². The cool roof is referred to as a roof with higher albedo and emissivity than conventional roofs¹³. Many previous studies showed that the application of cool roofs effectively decreases the UHI intensity^{14–22}. For instance, He et al.¹⁵ examined cool-roof effects on the UHI in 16 cities in the Yangtze River Delta, China and showed that increasing roof albedo from 0.12 to 0.65 decreases urban 2-m temperature by up to 1.19 °C in summer. Reed and Sun²⁰ investigated cool-roof scenarios in Kansas City, U.S. and revealed that increasing roof albedo from 0.3 to 0.8 decreases the UHI intensity by up to 0.64 °C. Baik et al.¹⁴ examined cool-roof effects on urban thermal and wind environments during a record-breaking heat wave event in Seoul, South Korea and showed that increasing roof albedo from 0.2 to 0.7 decreases urban 2-m temperature by up to 1.0 °C. Zonato et al.²³ examined how cool-roof effects on the UHI differ depending on urban morphology and season through idealized simulations. They revealed that cool-roof effects on the UHI are enhanced with increasing the plan area of buildings and with decreasing building height and are stronger by about 10 times in summer than in winter.

Meanwhile, some previous studies showed that the application of cool roofs may reduce ventilation and therefore worsen air quality in urban areas^{24–28}. Wang et al.²⁶ examined cool-roof effects on the concentration of particulate matter with a diameter less than 2.5 μm ($\text{PM}_{2.5}$) in North China and revealed that increasing roof

School of Earth and Environmental Sciences, Seoul National University, 08826 Seoul, South Korea. ✉email: jjbaik@snu.ac.kr

albedo from 0.2 to 0.9 increases urban $\text{PM}_{2.5}$ concentration in the daytime by up to 42%. Zhong et al.²⁸ evaluated cool-roof effects on heavy ozone (O_3) pollution events in Shanghai, China and showed that the application of cool roofs increases urban near-surface O_3 concentration by suppressing the development of planetary boundary layer (PBL). On the other hand, it was also reported that the application of cool roofs may decrease urban O_3 concentration by reducing the rates of temperature-dependent reactions and energy consumption which causes the emission of O_3 precursors^{29,30}.

The alleviation of the UHI is a beneficial effect of cool roofs in terms of thermal discomfort in warm seasons, but the air stagnation and thus the deterioration of air quality are side effects that could be accompanied by the application of cool roofs³¹. In order to find an appropriate trade-off between the UHI mitigation and its side effects on air quality, how the UHI responds to an increase in roof albedo and how this affects urban air quality should be well understood but are still open questions. Several case studies reported an almost linear relationship between the UHI intensity and roof albedo^{27,32,33}. For instance, Li et al.³² simulated a heat wave event in Baltimore, U.S. using the Weather Research and Forecasting (WRF) model and revealed that the UHI intensity almost linearly decreases with increasing roof albedo. On the other hand, a few case studies revealed a nonlinear relationship between the UHI intensity and roof albedo^{16,17}. Imran et al.¹⁶ examined three cool-roof scenarios with roof albedos of 0.50, 0.70, and 0.85 during a heat wave event in Melbourne, Australia and showed that the increase in roof albedo from 0.50 to 0.70 has a larger UHI mitigation effect than that from 0.70 to 0.85.

Despite many attempts to understand the relationships of the UHI and urban air quality with roof albedo in various cities, most previous studies have examined only a few roof albedo cases or a limited range of roof albedo. Furthermore, the urban breeze circulation (UBC), which is a mesoscale circulation induced by the UHI³⁴, is expected to be significantly modified as the roof albedo changes²⁸, but the relationship between the UBC and roof albedo has been rarely examined. Given its significant influences on local circulations and air quality in urban areas^{35,36}, a detailed examination of changes in the UBC with roof albedo could enhance the understanding of roof albedo effects on urban environments. Thus, in this study, we aim to systematically examine how the UHI and UBC respond to an increase in roof albedo and how this affects urban air pollutant dispersion. For this, idealized ensemble simulations with various roof albedos from 0.10 to 0.95 are performed. The idealized simulations enable to examine various roof albedo cases because of their low computational cost²³. Furthermore, in the idealized simulations, the interferences of synoptic and local features can be excluded³⁷, making it possible to find essentially important physical processes for changes in the UHI, UBC, and urban air pollutant dispersion with roof albedo.

Methods

This study uses the WRF model version 4.1.3³⁸ to perform the idealized ensemble simulations. This study considers an idealized two-dimensional (x - z) computational domain with the horizontal and vertical sizes of 500 km and 7 km, respectively. The 250-m horizontal grid interval is employed, and the vertical grid interval increases with height. The height of the first model level is 13 m, and the number of vertical layers is 66. The periodic lateral boundary conditions are adopted, and the Rayleigh damping³⁹ is applied above 5 km. An urban area is considered in the middle area of the domain, and its size is 20 km. The land use types of the urban area and surrounding rural area are industrial/commercial area and cropland/woodland mosaic, respectively. The midlatitude (30°N) is considered.

To better simulate urban land surface processes, the Seoul National University Urban Canopy Model (SNUUCM)⁴⁰ is coupled with the WRF model. The SNUUCM is one of the single-layer urban canopy models (UCMs) that can be implemented in atmospheric models. The key features of the SNUUCM are that two building walls (sunlit and shaded walls) are separately treated and that the effects of reference wind direction and canyon aspect ratio are considered in calculating the canyon wind speed⁴⁰. The SNUUCM well simulates surface energy fluxes and the surface temperatures of urban facets observed in many urban sites^{40–43}. In the urban grid, the fraction of built-up area is set to 0.9, and the fraction of natural area is set to 0.1. To simulate land surface processes in the rural grid and the natural area fraction in the urban grid, the unified Noah land surface model⁴⁴ is used. Both road width and building height are set to 10 m, the urban canyon aspect ratio being 1.0⁴⁵. The roof width is set to 10 m as well. The emissivity, heat capacity, thermal conductivity, and roughness length of roof are set to 0.95, 1.0 MJ m⁻³ K⁻¹, 0.67 J m⁻¹ s⁻¹ K⁻¹, and 0.01 m, respectively. The albedos/emissivities of both road and walls are 0.18/0.95, and the heat capacity, thermal conductivity, and roughness length of road (walls) are 1.4 MJ m⁻³ K⁻¹ (1.0 MJ m⁻³ K⁻¹), 0.40 J m⁻¹ s⁻¹ K⁻¹ (0.67 J m⁻¹ s⁻¹ K⁻¹), and 0.01 m (0.0001 m), respectively⁴⁵. For PBL and surface layer parameterizations, the Yonsei University PBL scheme⁴⁶ and the revised MM5 similarity scheme⁴⁷ are employed, respectively. For cloud microphysics parameterization, the WRF single-moment 6-class scheme⁴⁸ is used. Note that cloud microphysical processes do not affect our main results since the clear-sky (cloudless) conditions are considered in this study. For radiation parameterizations, the Dudhia shortwave radiation scheme⁴⁹ and the Rapid Radiative Transfer Model (RRTM) longwave radiation scheme⁵⁰ are used. To investigate the impact of increasing roof albedo on urban air pollutant dispersion, the WRF model is coupled with chemistry⁵¹, a passive tracer option being used. In this option, the carbon monoxide (CO) is treated as a passive tracer and its transport is simulated.

Total 18 experiments are conducted by applying different roof albedos from 0.10 to 0.95 with an interval of 0.05. For initial sounding, a linear potential temperature (water vapor mixing ratio) profile in which the value is 298.15 K/333.15 K (3.00 g kg⁻¹/0.67 g kg⁻¹) at the surface/model top height is considered for all the experiments. The initial background wind speed is set to 0 m s⁻¹ in all vertical layers, and the Coriolis parameter is set to 0 s⁻¹. The initial soil moisture content is set to 0.3 m³ m⁻³ in all soil layers. The initial passive tracer (CO) concentration is set to 400 ppb at the first model level in the urban area. A diurnally varying passive tracer emission from the surface is considered in the urban area. Its diurnal variation is based on that of the traffic volume in Seoul in 2023 (<https://topis.seoul.go.kr>), and the daily mean emission rate is 3 × 10⁻⁷ g m⁻² s⁻¹.

(Supplementary Fig. S1). For each experiment, the ensemble simulations are performed following Tabassum et al.³⁷: 10 ensemble members are considered, and random potential temperature perturbations within $[-0.1 \text{ K}, 0.1 \text{ K}]$ are applied to the three lowest model levels. The model integration period is from 0000 LST 21 June to 0000 LST 23 June (a summer period). For analysis, the ensemble-mean results for the 24-h period starting from 0000 LST 22 June are used. The UHI intensity is defined as the 2-m temperature averaged over all urban grids minus the 2-m temperature averaged over all rural grids. Referring to Tabassum et al.³⁷, the UBC intensity is defined as the maximum horizontal wind speed in the lower half of the PBL. The main analyses are conducted for the daytime which is defined as the period from 1200 to 1700 LST.

Results and discussions

Changes in the UHI, UBC, and urban tracer concentration with roof albedo

Figure 1 shows the daytime mean UHI intensity, UBC intensity, urban PBL height, and urban passive tracer concentration at the first model level as a function of roof albedo (α_r). As can be expected, the daytime mean UHI intensity monotonically decreases with increasing α_r . As α_r increases from 0.20 to 0.65, the daytime mean UHI intensity decreases from 1.26 °C to 0.67 °C (by 47%). This UHI mitigation effect is comparable to those reported in previous studies^{18–21}. It is notable that the rate of decrease in the UHI intensity overall increases with increasing α_r for $0.10 \leq \alpha_r < 0.80$. For $\alpha_r \geq 0.80$, the daytime mean UHI intensity very slightly changes with α_r . Thus, in the present idealized simulations, the daytime UHI intensity nonlinearly changes with α_r : The effect of increasing α_r on the UHI mitigation is enhanced as α_r increases and becomes very weak when α_r is very high ($\alpha_r \geq 0.80$). The nonlinear change in the UHI intensity with α_r is closely associated with those in the daytime mean urban 2-m temperature (Supplementary Fig. S2). The daytime mean rural 2-m temperature very slightly changes with α_r (Supplementary Fig. S2).

As the daytime mean UHI intensity decreases with increasing α_r , the daytime mean UBC intensity similarly decreases as α_r increases (Fig. 1b). The similar response of the UBC to an increase in α_r as that of the UHI is

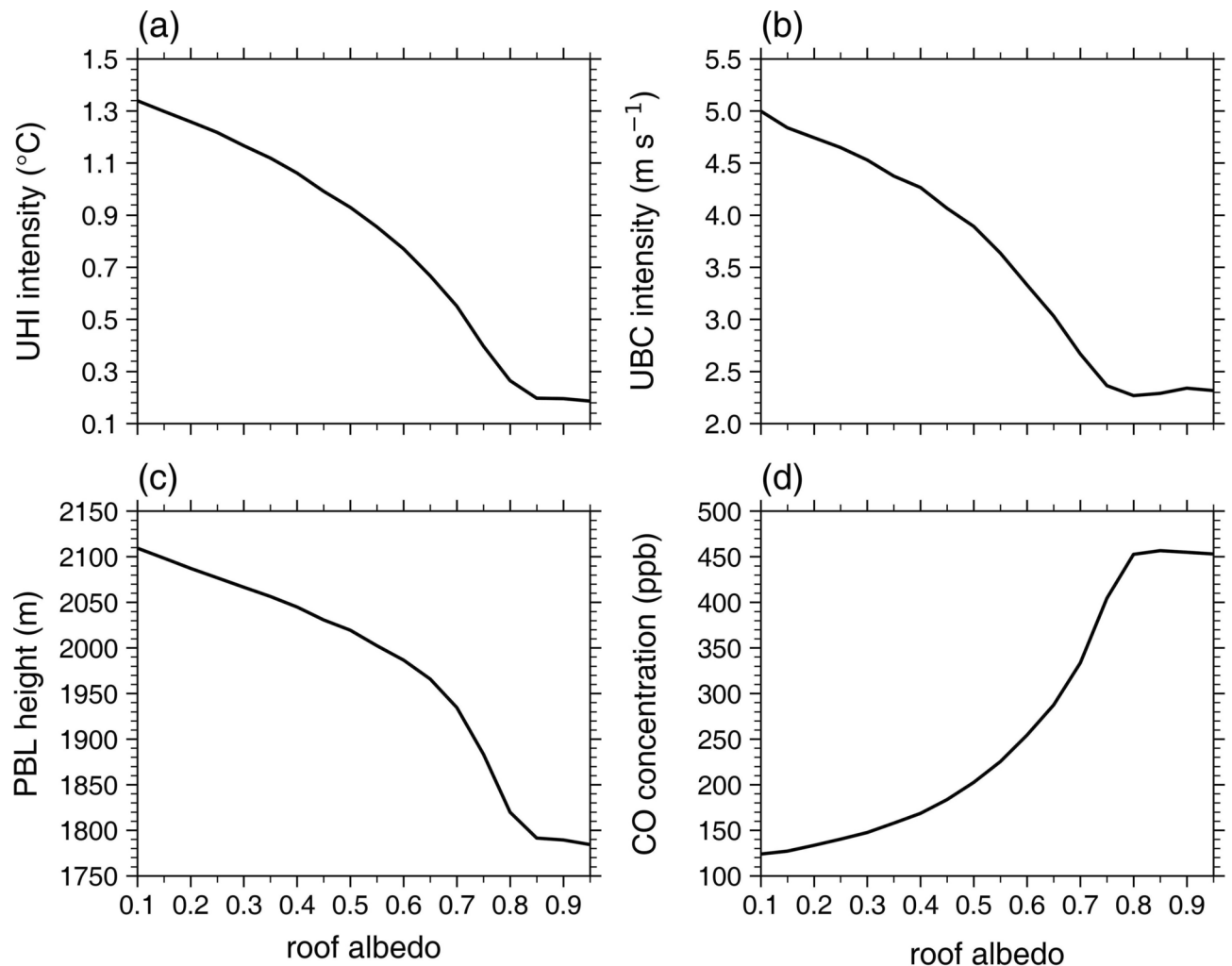


Fig. 1. Daytime mean (a) urban heat island intensity, (b) urban breeze circulation intensity, (c) urban planetary boundary layer height, and (d) urban passive tracer (carbon monoxide) concentration at the first model level as a function of roof albedo.

due to the fact that the UBC is driven by the UHI. As α_r increases from 0.20 to 0.65, the daytime mean UBC intensity decreases from 4.7 m s^{-1} to 3.0 m s^{-1} (by 36%). As α_r increases, the daytime mean urban PBL height also monotonically decreases (Fig. 1c). This is attributed to the decrease in urban near-surface air temperature with increasing α_r (Supplementary Fig. S2) which stabilizes the urban PBL⁵². The decrease in daytime PBL height with increasing α_r has been shown in previous studies^{16,17}. As α_r increases from 0.20 to 0.65, the daytime mean urban PBL height decreases from 2087 m to 1966 m (by 6%). The daytime mean urban PBL height exhibits a nearly linear decrease with increasing α_r for $0.10 \leq \alpha_r \leq 0.30$, but the rate of decrease in the PBL height overall increases with increasing α_r for $0.30 < \alpha_r < 0.80$. For $\alpha_r \geq 0.80$, the daytime mean urban PBL height very slightly changes with α_r .

The daytime mean urban near-surface tracer concentration generally exhibits a substantial increase with increasing α_r (Fig. 1d). Given that the UBC transports relatively clean rural air to the urban area and relatively polluted urban air to the rural area, this is primarily due to the overall decrease in the UBC intensity with increasing α_r (Fig. 1b). Furthermore, the decrease in the urban PBL height with increasing α_r (Fig. 1c), which indicates the reduction in the vertical turbulent mixing⁵³, is also responsible for the overall increase in the urban tracer concentration with increasing α_r . As α_r increases from 0.20 to 0.65, the daytime mean urban near-surface tracer concentration considerably increases from 133 ppb to 287 ppb (by 115%). Like the UHI intensity, it is noticeable that the rate of increase in the urban tracer concentration generally increases with increasing α_r for $0.10 \leq \alpha_r < 0.80$ and the urban tracer concentration exhibits no significant change with α_r for $\alpha_r \geq 0.80$. This indicates that in the present simulations, the daytime urban tracer concentration also nonlinearly changes with α_r : The negative effect of increasing α_r on urban air pollutant dispersion is enhanced as α_r increases and becomes very weak when α_r is very high ($\alpha_r \geq 0.80$). This result is reproduced in the experiments with the 1000-m horizontal grid interval which does not belong to the gray-zone resolutions⁵⁴ (Supplementary Fig. S3). Overall, the simulated worsening of urban air quality, indicated by the increase in the tracer concentration, with increasing α_r is notably strong. In the present simulations, the UBC is the sole local circulation affecting the dispersion of air pollutants. In the presence of prevailing background winds and/or other local circulations, the degree of changes in urban air pollutant concentrations with α_r could greatly differ^{24,28}. Furthermore, for secondary air pollutants (e.g., O_3 , $\text{PM}_{2.5}$), changes in various temperature-dependent chemical reactions with α_r can affect the impact of increasing α_r on pollutant concentrations in complex ways^{27,55}, which deserves further investigations.

How increasing α_r affects the structures of the UBC and urban PBL is examined in detail. Figure 2 shows the daytime mean fields of wind vectors and passive tracer concentration and the daytime mean vertical profiles of urban potential temperature and urban tracer concentration for $\alpha_r = 0.20$ and 0.65. For $\alpha_r = 0.20$, the UBC is clearly seen, with the converging flows toward the urban area in the lower PBL, the ascending flows at the urban center, and the diverging flows from the urban area in the upper PBL (Fig. 2a). The horizontal size of the UBC is 125 km, and the vertical size of the UBC is 3.0 km at the urban center. The maximum vertical velocity at the urban center is 4.1 m s^{-1} . Along the well-developed UBC, the tracer is widely dispersed. As α_r increases to 0.65, the weakening and contraction of the UBC are evident (Fig. 2c). The horizontal size of the UBC decreases to 51 km, and the vertical size of the UBC decreases to 2.6 km at the urban center. Furthermore, the maximum vertical velocity at the urban center considerably decreases to 0.5 m s^{-1} . As a result, the dispersion of the tracer is greatly inhibited, the tracer being accumulated within the PBL at and near the urban center.

The increase in α_r leads to significant changes in urban potential temperature and tracer concentration throughout the PBL (Fig. 2b and d). For $\alpha_r = 0.20$, a statically unstable layer in which the rate of change in potential temperature with height is -0.014 K m^{-1} is found below $z = 40 \text{ m}$ (Fig. 2b). Above $z \sim 0.1 \text{ km}$, a well-mixed layer is developed up to $z \sim 2.0 \text{ km}$. The daytime mean potential temperature averaged over the well-mixed layer is 305.5 K. As α_r increases to 0.65, the static instability below $z = 40 \text{ m}$ (-0.009 K m^{-1}) decreases and the top height of the well-mixed layer decreases to $z \sim 1.8 \text{ km}$. This inhibits urban air pollutants from being dispersed away from the surface, contributing to the increase in the urban tracer concentration (Fig. 1d). The daytime mean urban potential temperature averaged over the well-mixed layer decreases by 0.6 K, which is comparable to the decrease in the UHI intensity (Fig. 1a). This urban PBL cooling by the increase in α_r agrees with previous studies^{16,17,31}. Meanwhile, as α_r increases from 0.20 to 0.65, the urban tracer concentration increases throughout the PBL (Fig. 2d). The daytime mean urban tracer concentration averaged over the well-mixed layer increases from 118 ppb to 270 ppb.

Changes in roof surface temperature and roof surface energy fluxes with roof albedo and their associations with the nonlinear change in UHI intensity

Given changes in α_r directly alter the roof surface energy balance and thus roof surface temperature, changes in UHI intensity with α_r are primarily associated with those in roof surface temperature and roof surface energy fluxes. In this subsection, to elucidate the nonlinear change in the daytime UHI intensity with α_r (Fig. 1a), how the roof surface temperature and roof surface energy fluxes change with α_r is examined. Figure 3 shows the daytime mean roof surface temperature, roof sensible heat flux, roof latent heat flux, and roof storage heat flux as a function of α_r . The daytime mean roof surface temperature monotonically decreases with increasing α_r (Fig. 3a). As α_r increases from 0.20 to 0.65, the daytime mean roof surface temperature decreases from 39.0°C to 33.5°C . For $0.10 \leq \alpha_r < 0.80$, the rate of decrease in the roof surface temperature overall increases with increasing α_r , in line with that in the urban 2-m temperature (Supplementary Fig. S2). This indicates that the nonlinear decrease in the UHI intensity with increasing α_r for $0.10 \leq \alpha_r < 0.80$ is associated with that in the roof surface temperature. The rate of decrease in the roof surface temperature also increases with increasing α_r for $\alpha_r \geq 0.80$, but it is well seen that the daytime mean roof surface temperature is notably lower than the daytime mean urban 2-m temperature (Fig. 3a). The daytime mean roof sensible heat flux almost linearly decreases with increasing α_r for $0.10 \leq \alpha_r < 0.80$ (Fig. 3b). As α_r increases from 0.20 to 0.65, the daytime mean roof sensible heat flux

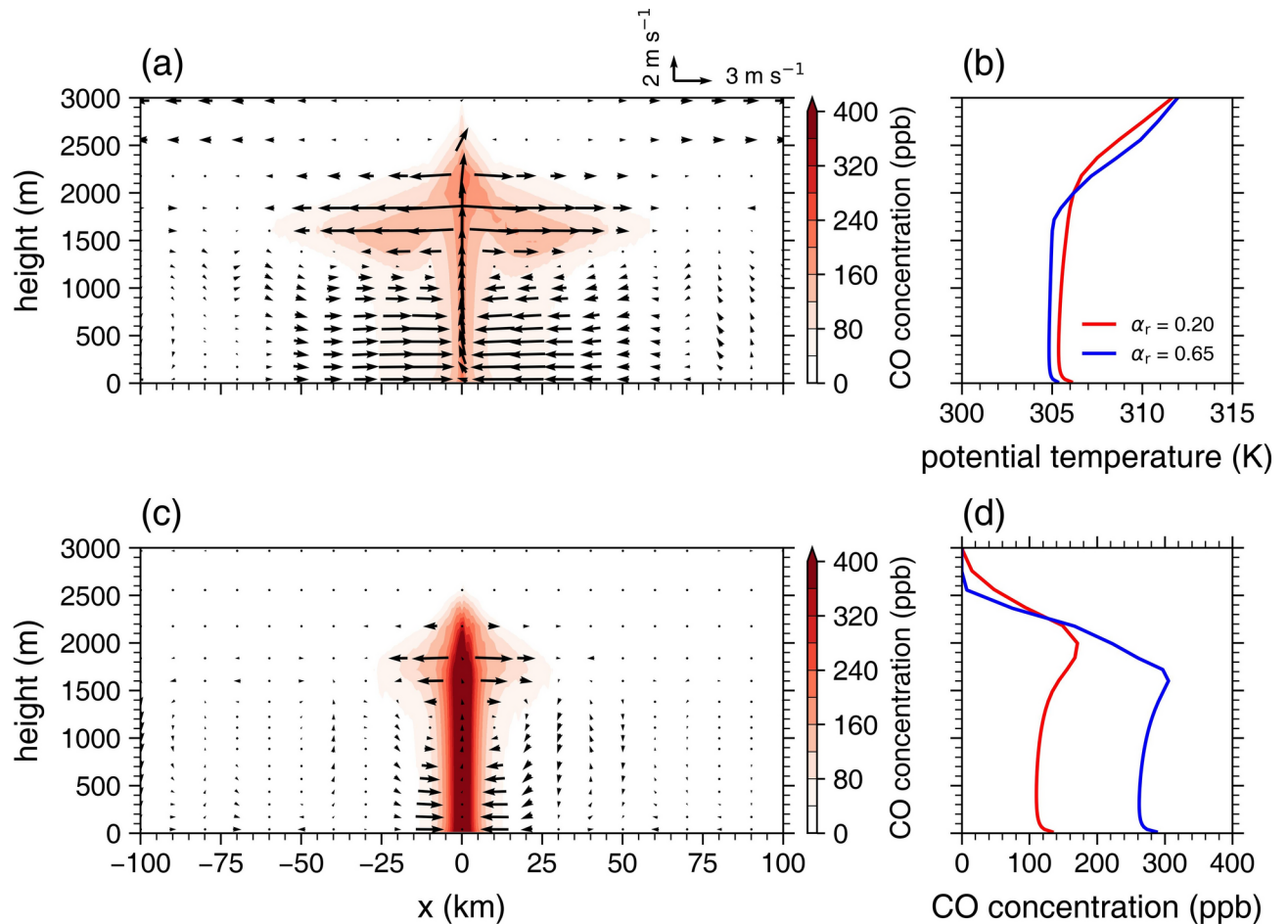


Fig. 2. (a) Daytime mean field of passive tracer (carbon monoxide) concentration (shade) and wind vectors (arrow) for a roof albedo of 0.20. (b) Daytime mean vertical profiles of urban potential temperature for roof albedos of 0.20 (red) and 0.65 (blue). (c) Same as (a) except for a roof albedo of 0.65. (d) Daytime mean vertical profiles of urban passive tracer concentration for roof albedos of 0.20 (red) and 0.65 (blue).

decreases from 500 W m^{-2} to 131 W m^{-2} . For $\alpha_r \geq 0.80$, the daytime mean roof sensible heat flux is very small and very slightly changes with α_r . Particularly, the daytime mean roof sensible heat flux is negative for $\alpha_r \geq 0.85$, indicating the sensible heat transfer from the urban near-surface air to the roof surface. Thus, as the roof surface temperature becomes notably lower than the urban near-surface air temperature in the daytime for $\alpha_r \geq 0.80$ (Fig. 3a), the upward sensible heat flux from the roof hardly appears and does not significantly change with α_r (Fig. 3b). Furthermore, due to the notably lower roof surface temperature than the urban near-surface air temperature, the net radiative heat transfer from the roof surface to the urban near-surface air can also be greatly inhibited. These may greatly weaken the decrease in the UHI intensity with increasing α_r for $\alpha_r \geq 0.80$ (Fig. 1a). Meanwhile, the daytime mean roof latent heat flux is 0 W m^{-2} for all α_r (Fig. 3c). This is due to the lack of roof vegetation. Note that the urban latent heat flux arises from the natural area fraction in the urban grid.

The daytime mean roof storage heat flux exhibits distinct changes from the roof sensible and latent heat fluxes as α_r increases (Fig. 3d). The daytime mean roof storage heat flux is positive for all α_r , indicating that the heat is conducted from the roof surface to the roof subsurface (heat storing). Interestingly, for $0.10 \leq \alpha_r < 0.80$, the daytime mean roof storage heat flux overall increases with increasing α_r . As α_r increases from 0.20 to 0.65, the daytime mean roof storage heat flux increases from 16 W m^{-2} to 33 W m^{-2} . Furthermore, the rate of increase in the roof storage heat flux overall increases with increasing α_r . Since the heat storing from the roof surface into the roof subsurface inhibits the roof surface heating by solar radiation, the overall increasing rate of increase in the roof storage heat flux with increasing α_r for $0.10 \leq \alpha_r < 0.80$ is responsible for that of decrease in the roof surface temperature (Fig. 3a). On the other hand, for $\alpha_r \geq 0.80$, the daytime mean roof storage heat flux overall linearly decreases with increasing α_r (Fig. 3d).

Changes in roof storage heat flux with α_r are further examined in Fig. 4. Figure 4 shows the diurnal variations of roof storage heat flux for $\alpha_r = 0.20, 0.50, 0.80$, and 0.95 . For $\alpha_r = 0.20$, the maximum roof storage heat flux is 186 W m^{-2} and appears at 0820 LST (Fig. 4). This shows that the heat storing into the roof subsurface mainly occurs in the morning. It is well known that the net radiation at the urban surface is primarily transferred into storage heat flux in the morning and into sensible heat flux in the daytime⁵⁶. As α_r increases from 0.20 to 0.50, the mean roof storage heat flux in the morning (from 0600 to 1100 LST) decreases by 27 W m^{-2} while the daytime

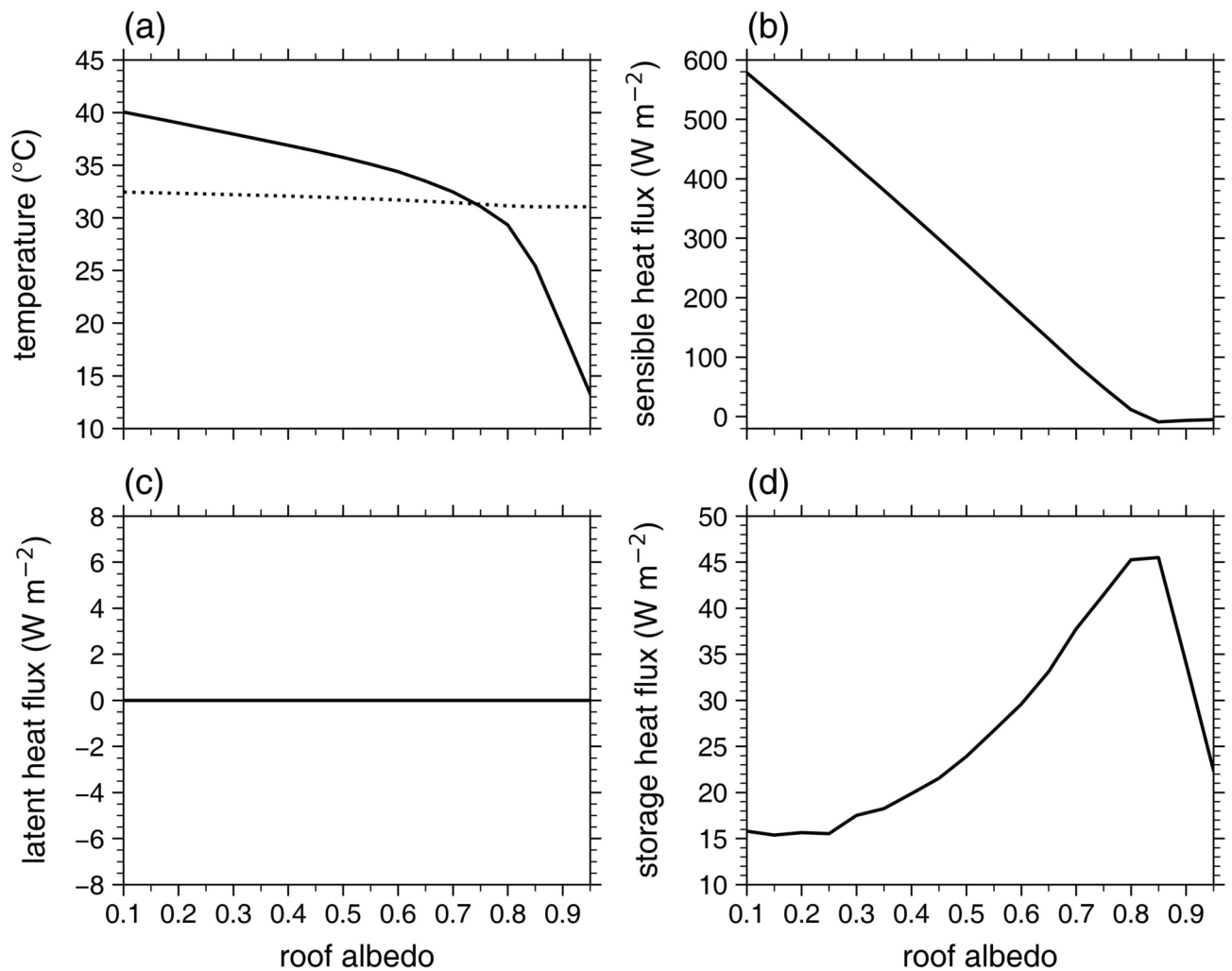


Fig. 3. Daytime mean (a) roof surface temperature, (b) roof sensible heat flux, (c) roof latent heat flux, and (d) roof storage heat flux as a function of roof albedo. The dotted line in (a) indicates the daytime mean urban 2-m temperature as a function of roof albedo.

mean roof storage heat flux increases by 8 W m^{-2} . This indicates that the period when the heat storing mainly occurs is delayed as α_r increases. As α_r further increases from 0.50 to 0.80, the mean roof storage heat flux in the morning further decreases by 49 W m^{-2} while the daytime mean roof storage heat flux further increases by 21 W m^{-2} . The rate of decrease in the mean roof storage heat flux in the morning overall increases with increasing α_r for $0.10 \leq \alpha_r < 0.80$ (Supplementary Fig. S4), similar to the rate of increase in the daytime mean roof storage heat flux (Fig. 3d). Thus, the above results suggest that for $0.10 \leq \alpha_r < 0.80$, a low to moderately high α_r range, the increase in α_r may cause the solar radiation absorbed at the roof surface in the daytime to be more transferred into storage heat flux due to the lack of heat storing into the roof subsurface in the morning. On the other hand, as α_r increases from 0.80 to 0.95, the roof storage heat flux decreases in both morning and daytime and becomes very small (Fig. 4). This suggests that for $\alpha_r \geq 0.80$, a very high α_r range, the increase in α_r no more increases roof storage heat flux in the daytime because of too small amount of solar radiation absorbed at the roof surface in the daytime to be transferred into storage heat flux. For $\alpha_r \geq 0.80$, the roof storage heat flux overall linearly decreases with increasing α_r in both morning and daytime (Fig. 3d and Supplementary Fig. S4). It should be noted that the value of α_r from which the change in the roof storage heat flux with α_r differs could vary with urban thermal and morphological characteristics and background meteorological conditions. To understand the physical mechanisms behind changes in roof surface energy fluxes with α_r , further examinations for various urban configurations and meteorological conditions are needed.

Finally, to examine how changes in the UHI intensity, UBC intensity, and urban tracer concentration with α_r differ depending on UCMs, additional experiments are performed by using a single-layer UCM (SLUCM) developed by Kusaka et al.⁵⁷ instead of the SNUUCM. Figure 5 is the same as Fig. 1 except for the experiments with the SLUCM. Compared to the experiments with the SNUUCM, the daytime mean UHI intensity in the experiments with the SLUCM is weaker for all α_r and more decreases with increasing α_r (Fig. 5a). The daytime mean UHI intensity becomes negative for $\alpha_r \geq 0.70$, indicating the urban cool island. Due to this, the reversed UBC appears for $\alpha_r \geq 0.70$ and its intensity increases with increasing α_r (Fig. 5b). As α_r increases, the daytime

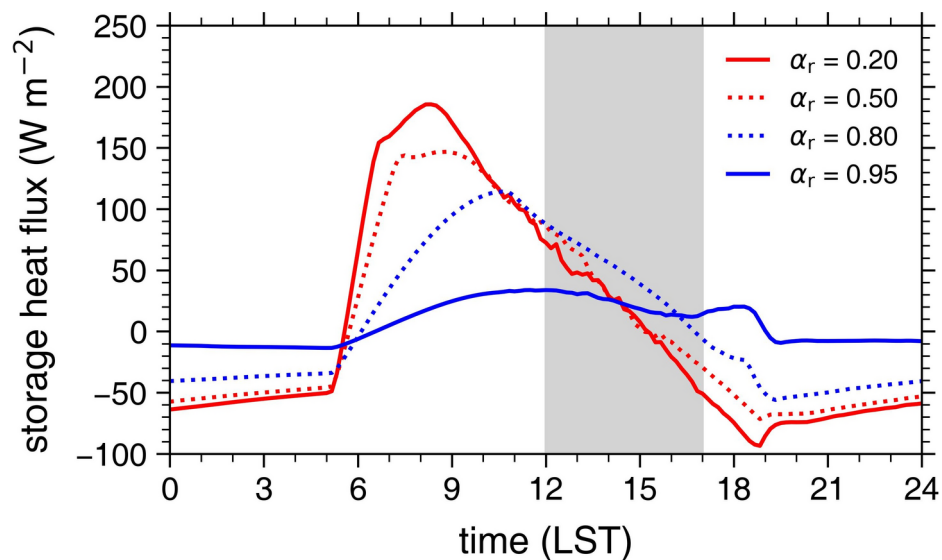


Fig. 4. Diurnal variations of roof storage heat flux for roof albedos of 0.20 (red solid line), 0.50 (red dotted line), 0.80 (blue dotted line), and 0.95 (blue solid line). The shaded area indicates the daytime defined as the period between 1200 and 1700 LST.

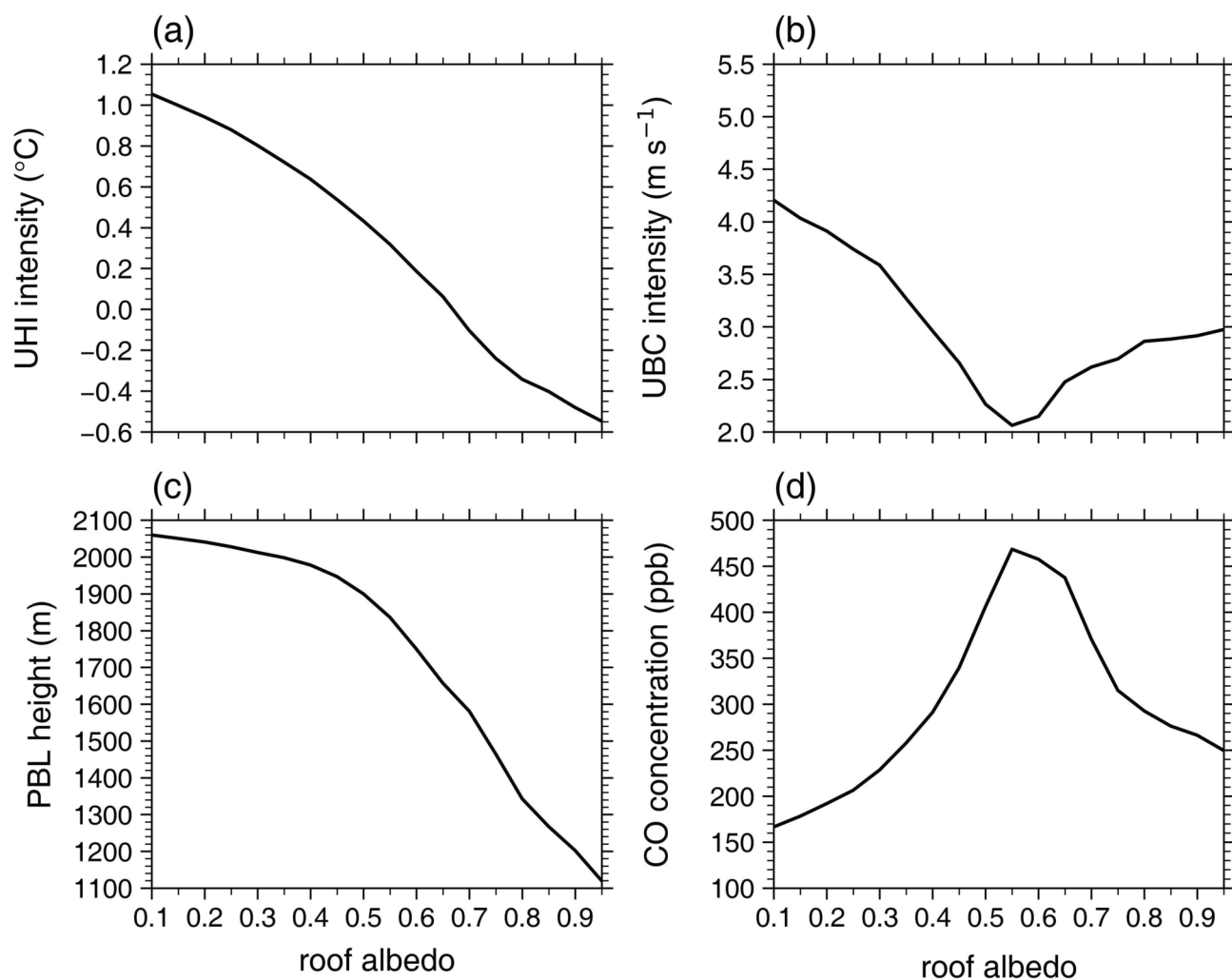


Fig. 5. Same as Fig. 1 except for the experiments with the SLUCM.

mean urban PBL height in the experiments with the SLUCM also more decreases than that in the experiments with the SNUUCM (Fig. 5c). The daytime mean urban near-surface tracer concentration increases as the UBC intensity decreases (Fig. 5d), showing a maximum concentration when the UBC intensity is weakest ($\alpha_r = 0.55$). Interestingly, the nonlinearity of change in the UHI intensity with α_r is relatively weak in the experiments with the SLUCM (Fig. 5a). Furthermore, the energy partitioning and changes in roof surface energy fluxes with α_r in the experiments with the SLUCM are quite different from those in the experiments with the SNUUCM. In comparison with the experiments with the SNUUCM, the daytime roof sensible heat flux is generally smaller in the experiments with the SLUCM, while the daytime roof storage heat flux is generally larger (Supplementary Fig. S5). It is also notable that for $0.10 \leq \alpha_r < 0.80$, the daytime roof storage heat flux in the experiments with the SLUCM does not increase with increasing α_r and the rate of decrease in the daytime roof sensible heat flux overall slightly decreases with increasing α_r (Supplementary Fig. S5). These differing energy partitioning and changes in roof surface energy fluxes depending on the UCMs make changes in UHI intensity with α_r and their associated physical processes vary. These results imply the necessity of evaluating how the UHI intensity changes with α_r with various UCMs to better understand the relationship between the UHI and α_r .

Conclusions

In this study, changes in the UHI, UBC, and urban air pollutant dispersion with α_r are systematically examined through idealized ensemble simulations with the WRF model coupled with the SNUUCM. As α_r increases, the daytime mean UHI intensity, UBC intensity, and urban PBL height overall decrease and the daytime mean urban near-surface passive tracer concentration generally exhibits a substantial increase with increasing α_r . The daytime mean UHI intensity, UBC intensity, and urban tracer concentration nonlinearly change with α_r . For $0.10 \leq \alpha_r < 0.80$, the effects of increasing α_r on the UHI, UBC and urban air pollutant dispersion are overall enhanced as α_r increases. For $\alpha_r \geq 0.80$, the roof surface temperature is notably lower than the urban near-surface air temperature in the daytime, the effects of increasing α_r on the UHI, UBC and urban air pollutant dispersion being very weak. The nonlinear changes in the UHI intensity, UBC intensity, and urban tracer concentration with α_r are associated with the changes in the roof surface temperature and roof surface energy fluxes with α_r , as presented in Fig. 6.

In this study, it is found that changes in the UHI intensity, UBC intensity, and urban tracer concentration with α_r for $0.10 \leq \alpha_r < 0.80$ are considerably different from those for $\alpha_r \geq 0.80$. However, the value of α_r from which these changes differ may vary depending on urban thermal and morphological characteristics and background meteorological conditions. To advance the understanding of changes in UHI intensity with α_r and their associated physical processes, further investigations with simulations under different urban characteristics, seasons, and latitudes are required. Furthermore, it should be noted that changes in UHI intensity with α_r and their associated physical processes also vary depending on UCMs. This is attributed to that each UCM simulates

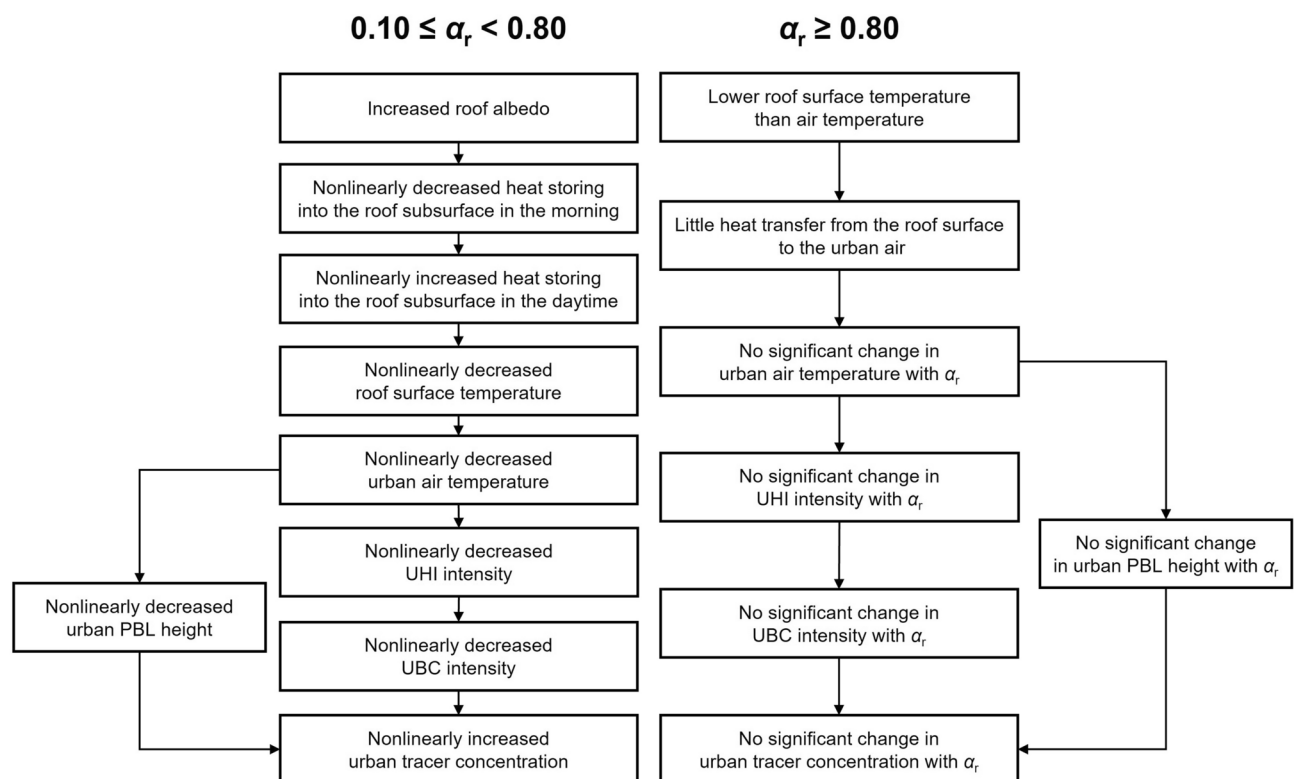


Fig. 6. Schematic diagram of the impacts of increasing roof albedo on the urban heat island, urban breeze circulation, and urban tracer concentration found in the idealized ensemble simulations.

urban turbulent and storage heat fluxes differently for given incoming solar radiation and meteorological conditions. Given this aspect, the use of various UCMs could help to better understand the relationship between the UHI and α_p .

Data availability

The datasets generated during and/or analyzed during the current study are available from the corresponding author on reasonable request.

Received: 28 July 2024; Accepted: 17 October 2024

Published online: 22 October 2024

References

1. Liu, Z., He, C., Zhou, Y. & Wu, J. How much of the world's land has been urbanized, really? A hierarchical framework for avoiding confusion. *Landsc. Ecol.* **29**, 763–771 (2014).
2. United Nations, Department of Economic and Social Affairs, Population Division. *World Urbanization Prospects: The 2018 Revision* (ST/ESA/SER.A/420). <https://population.un.org/wup/Publications/Files/WUP2018-Report.pdf> (2019).
3. Chapman, S., Watson, J. E. M., Salazar, A., Thatcher, M. & McAlpine, C. A. The impact of urbanization and climate change on urban temperatures: A systematic review. *Landsc. Ecol.* **32**, 1921–1935 (2017).
4. Grimmond, S. Urbanization and global environmental change: Local effects of urban warming. *Geogr. J.* **173**, 83–88 (2007).
5. Oke, T. R. The energetic basis of the urban heat island. *Q. J. R. Meteorol. Soc.* **108**, 1–24 (1982).
6. Heaviside, C., Macintyre, H. & Vardoulakis, S. The urban heat island: Implications for health in a changing environment. *Curr. Environ. Health Rep.* **4**, 296–305 (2017).
7. Tan, J. et al. The urban heat island and its impact on heat waves and human health in Shanghai. *Int. J. Biometeorol.* **54**, 75–84 (2010).
8. Lowe, S. A. An energy and mortality impact assessment of the urban heat island in the US. *Environ. Impact Assess. Rev.* **56**, 139–144 (2016).
9. Milan, B. F. & Creutzig, F. Reducing urban heat wave risk in the 21st century. *Curr. Opin. Environ. Sustain.* **14**, 221–231 (2015).
10. Santamouris, M. Recent progress on urban overheating and heat island research. Integrated assessment of the energy, environmental, vulnerability and health impact. Synergies with the global climate change. *Energy Build.* **207**, 109482 (2020).
11. Deilami, K., Kamruzzaman, M. & Liu, Y. Urban heat island effect: A systematic review of spatio-temporal factors, data, methods, and mitigation measures. *Int. J. Appl. Earth Obs. Geoinf.* **67**, 30–42 (2018).
12. Rawat, M. & Singh, R. N. A study on the comparative review of cool roof thermal performance in various regions. *Energy Built Environ.* **3**, 327–347 (2022).
13. Tian, D., Zhang, J. & Gao, Z. The advancement of research in cool roof: Super cool roof, temperature-adaptive roof and crucial issues of application in cities. *Energy Build.* **291**, 113131 (2023).
14. Baik, J.-J., Lim, H., Han, B.-S. & Jin, H.-G. Cool-roof effects on thermal and wind environments during heat waves: A case modeling study in Seoul, South Korea. *Urban Clim.* **41**, 101044 (2022).
15. He, C. et al. Cool roof and green roof adoption in a metropolitan area: Climate impacts during summer and winter. *Environ. Sci. Technol.* **54**, 10831–10839 (2020).
16. Imran, H. M., Kala, J., Ng, A. W. M. & Muthukumar, S. Effectiveness of green and cool roofs in mitigating urban heat island effects during a heatwave event in the city of Melbourne in southeast Australia. *J. Clean. Prod.* **197**, 393–405 (2018).
17. Khorat, S. et al. Cool roof strategies for urban thermal resilience to extreme heatwaves in tropical cities. *Energy Build.* **302**, 113751 (2024).
18. Li, X.-X. & Norford, L. K. Evaluation of cool roof and vegetations in mitigating urban heat island in a tropical city, Singapore. *Urban Clim.* **16**, 59–74 (2016).
19. Mughal, M. O., Li, X.-X. & Norford, L. K. Urban heat island mitigation in Singapore: Evaluation using WRF/multilayer urban canopy model and local climate zones. *Urban Clim.* **34**, 100714 (2020).
20. Reed, K. & Sun, F. Investigating the potential for cool roofs to mitigate urban heat in the Kansas City metropolitan area. *Clim. Dyn.* **60**, 461–475 (2023).
21. Wang, X., Li, H. & Sodoudi, S. The effectiveness of cool and green roofs in mitigating urban heat island and improving human thermal comfort. *Build. Environ.* **217**, 109082 (2022).
22. Zhang, N., Chen, Y., Luo, L. & Wang, Y. Effectiveness of different urban heat island mitigation methods and their regional impacts. *J. Hydrometeorol.* **18**, 2991–3012 (2017).
23. Zonato, A. et al. Exploring the effects of rooftop mitigation strategies on urban temperatures and energy consumption. *J. Geophys. Res. Atmos.* **126**, e2021JD035002 (2021).
24. Epstein, S. A. et al. Air-quality implications of widespread adoption of cool roofs on ozone and particulate matter in southern California. *Proc. Natl. Acad. Sci. U. S. A.* **114**, 8991–8996 (2017).
25. Falasca, S. & Curci, G. Impact of highly reflective materials on meteorology, PM10 and ozone in urban areas: A modeling study with WRF-CHIMERE at high resolution over Milan (Italy). *Urban Sci.* **2**, 18 (2018).
26. Wang, F., Carmichael, G. R., Zhang, X., Xiao, X. & Gao, M. Pollution severity-regulated effects of roof strategies on China's winter PM_{2.5}. *npj Clim. Atmos. Sci.* **5**, 55 (2022).
27. Zhang, J. et al. Investigating the urban air quality effects of cool walls and cool roofs in Southern California. *Environ. Sci. Technol.* **53**, 7532–7542 (2019).
28. Zhong, T., Zhang, N. & Lv, M. A numerical study of the urban green roof and cool roof strategies' effects on boundary layer meteorology and ozone air quality in a megacity. *Atmos. Environ.* **264**, 118702 (2021).
29. Akbari, H., Pomerantz, M. & Taha, H. Cool surfaces and shade trees to reduce energy use and improve air quality in urban areas. *Sol. Energy* **70**, 295–310 (2001).
30. Jandaghian, Z. & Akbari, H. The effect of increasing surface albedo on urban climate and air quality: A detailed study for Sacramento, Houston, and Chicago. *Climate* **6**, 19 (2018).
31. Sharma, A. et al. Green and cool roofs to mitigate urban heat island effects in the Chicago metropolitan area: Evaluation with a regional climate model. *Environ. Res. Lett.* **11**, 064004 (2016).
32. Li, D., Bou-Zeid, E. & Oppenheimer, M. The effectiveness of cool and green roofs as urban heat island mitigation strategies. *Environ. Res. Lett.* **9**, 055002 (2014).
33. Lu, H. et al. Thermal effects of cool roofs and urban vegetation during extreme heat events in three Canadian regions. *Sust. Cities Soc.* **99**, 104925 (2023).
34. Hidalgo, J., Masson, V. & Pigeon, G. Urban-breeze circulation during the CAPITOUL experiment: Numerical simulations. *Meteorol. Atmos. Phys.* **102**, 243–262 (2008).
35. Ryu, Y.-H. & Baik, J.-J. Daytime local circulations and their interactions in the Seoul metropolitan area. *J. Appl. Meteorol. Climatol.* **52**, 784–801 (2013).

36. Ryu, Y.-H., Baik, J.-J., Kwak, K.-H., Kim, S. & Moon, N. Impacts of urban land-surface forcing on ozone air quality in the Seoul metropolitan area. *Atmos. Chem. Phys.* **13**, 2177–2194 (2013).
37. Tabassum, A., Hong, S.-H., Park, K. & Baik, J.-J. Impacts of changes in soil moisture on urban heat islands and urban breeze circulations: Idealized ensemble simulations. *Asia-Pac. J. Atmos. Sci.* **60**, 541–553 (2024).
38. Skamorock, W. C. et al. *A Description of the Advanced Research WRF Model Version 4*. NCAR Tech. Note NCAR/TN-556+STR (2019).
39. Klemp, J. B., Dudhia, J. & Hassiotis, A. D. An upper gravity-wave absorbing layer for NWP applications. *Mon. Weather Rev.* **136**, 3987–4004 (2008).
40. Ryu, Y.-H., Baik, J.-J. & Lee, S.-H. A new single-layer urban canopy model for use in mesoscale atmospheric models. *J. Appl. Meteorol. Climatol.* **50**, 1773–1794 (2011).
41. Grimmond, C. S. B. et al. The international urban energy balance models comparison project: First results from phase 1. *J. Appl. Meteorol. Climatol.* **49**, 1268–1292 (2010).
42. Grimmond, C. S. B. et al. Initial results from Phase 2 of the international urban energy balance model comparison. *Int. J. Climatol.* **31**, 244–272 (2011).
43. Lipson, M. J. et al. Evaluation of 30 urban land surface models in the Urban-PLUMBER project: Phase 1 results. *Q. J. R. Meteorol. Soc.* **150**, 126–169 (2024).
44. Chen, F. & Dudhia, J. Coupling an advanced land surface–hydrology model with the Penn State–NCAR MM5 modeling system. Part I: Model implementation and sensitivity. *Mon. Weather Rev.* **129**, 569–585 (2001).
45. Chen, F. et al. The integrated WRF/urban modelling system: Development, evaluation, and applications to urban environmental problems. *Int. J. Climatol.* **31**, 273–288 (2011).
46. Hong, S.-Y., Noh, Y. & Dudhia, J. A new vertical diffusion package with an explicit treatment of entrainment processes. *Mon. Weather Rev.* **134**, 2318–2341 (2006).
47. Jiménez, P. A. et al. A revised scheme for the WRF surface layer formulation. *Mon. Weather Rev.* **140**, 898–918 (2012).
48. Hong, S.-Y. & Lim, J.-O. The WRF single-moment 6-class microphysics scheme (WSM6). *J. Korean Meteorol. Soc.* **42**, 129–151 (2006).
49. Dudhia, J. Numerical study of convection observed during the Winter Monsoon Experiment using a mesoscale two-dimensional model. *J. Atmos. Sci.* **46**, 3077–3107 (1989).
50. Mlawer, E. J., Taubman, S. J., Brown, P. D., Iacono, M. J. & Clough, S. A. Radiative transfer for inhomogeneous atmospheres: RRTM, a validated correlated-k model for the longwave. *J. Geophys. Res. Atmos.* **102**, 16663–16682 (1997).
51. Grell, G. A. et al. Fully coupled “online” chemistry within the WRF model. *Atmos. Environ.* **39**, 6957–6975 (2005).
52. Zhang, N., Wang, X. & Peng, Z. Large-eddy simulation of mesoscale circulations forced by inhomogeneous urban heat island. *Bound.-Layer Meteorol.* **151**, 179–194 (2014).
53. Tang, G. et al. Mixing layer height and its implications for air pollution over Beijing, China. *Atmos. Chem. Phys.* **16**, 2459–2475 (2016).
54. Shin, H. H. & Hong, S.-Y. Representation of the subgrid-scale turbulent transport in convective boundary layers at gray-zone resolutions. *Mon. Weather Rev.* **143**, 250–271 (2015).
55. Han, B.-S., Baik, J.-J., Kwak, K.-H. & Park, S.-B. Effects of cool roofs on turbulent coherent structures and ozone air quality in Seoul. *Atmos. Environ.* **229**, 117476 (2020).
56. Oke, T. R., Mills, G., Christen, A. & Voogt, J. A. *Urban Climates* (Cambridge University Press, 2017).
57. Kusaka, H., Kondo, H., Kikegawa, Y. & Kimura, F. A simple single-layer urban canopy model for atmospheric models: Comparison with multi-layer and slab models. *Bound.-Layer Meteorol.* **101**, 329–358 (2001).

Acknowledgements

We are thankful to two anonymous reviewers for providing valuable comments which helped to significantly improve this article. This work was supported by the National Research Foundation of Korea (NRF) under grant 2021R1A2C1007044.

Author contributions

J.-J.B. designed and supervised this study. K.P. performed numerical simulations and visualization. All authors analyzed the simulation results. K.P. wrote the original draft. All authors reviewed and edited the manuscript. All authors read and approved the final version of the manuscript.

Declarations

Competing interests

The authors declare no competing interests.

Additional information

Supplementary Information The online version contains supplementary material available at <https://doi.org/10.1038/s41598-024-76935-4>.

Correspondence and requests for materials should be addressed to J.-J.B.

Reprints and permissions information is available at www.nature.com/reprints.

Publisher's note Springer Nature remains neutral with regard to jurisdictional claims in published maps and institutional affiliations.

Open Access This article is licensed under a Creative Commons Attribution 4.0 International License, which permits use, sharing, adaptation, distribution and reproduction in any medium or format, as long as you give appropriate credit to the original author(s) and the source, provide a link to the Creative Commons licence, and indicate if changes were made. The images or other third party material in this article are included in the article's Creative Commons licence, unless indicated otherwise in a credit line to the material. If material is not included in the article's Creative Commons licence and your intended use is not permitted by statutory regulation or exceeds the permitted use, you will need to obtain permission directly from the copyright holder. To view a copy of this licence, visit <http://creativecommons.org/licenses/by/4.0/>.

© The Author(s) 2024